Flow Measurement and Instrumentation 105 (2025) 102926

Contents lists available at ScienceDirect

Flow Measurement and Instrumentation

journal homepage: www.elsevier.com/locate/flowmeasinst

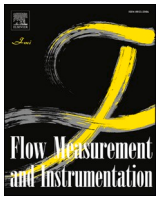

Convolutional neural networks to characterise particle suspensions from ultrasonic backscatter

Joseph J. Hartley [a,b], Lee F. Mortimer [a], Jeffrey Peakall [c], Richard A. Bourne [a], Jonathan M. Dodds [d], Martyn G. Barnes [b], Michael Fairweather [a], Timothy N. Hunter [a,*]

[a] School of Chemical and Process Engineering, University of Leeds, Leeds, LS2 9JT, UK
[b] Sellafield Ltd., Hinton House, Birchwood, WA3 6GR, UK
[c] School of Earth and Environment, University of Leeds, Leeds, LS2 9JT, UK
[d] United Kingdom National Nuclear Laboratory, Workington, CA13 3YQ, UK

ARTICLE INFO

Keywords:
Suspension
Particle size
Acoustic backscatter
Machine learning
ANN
CNN

ABSTRACT

Ultrasonic backscatter has been used extensively across many applications to characterise suspended particles. It is of particular interest in nuclear decommissioning, as it allows online characterisation without the need to sample, or even contact the suspension in some cases. Industrial processes often utilise dynamic changes to suspended particle concentrations and particle size distributions (PSDs), and as such, characterisation of both simultaneously would be advantageous. At present, there is limited scope within existing analytical methods to achieve this, where the concentration or PSD of the target system must be known to calculate the other. Machine learning (ML) is a method that when trained on representative data, can use non-linear multi-variable minimisations to estimate both concentration and PSD simultaneously and, as such, this study aims to demonstrate that an artificial neural network (ANN) and convolutional neural network (CNN) can accomplish this. A training library of nine spherical glass bead suspension systems, comprising of variable median particle size and coefficient of variation, across six concentrations was compiled using a commercial backscatter instrument at 2 and 4 MHz. The hyperparameters of an ANN and CNN were optimised on these acoustic profiles, before being used to predict median particle size, coefficient of variation, and concentration from acoustic profiles at 2 and 4 MHz of two "unknown" suspensions. While neither the ANN or CNN predictions proved to be successful for estimating the coefficient of variation, moderate agreement between predicted and true values were found for median particle size and concentration from the ANN, while the CNN achieved good agreement for median particle size and very good agreement when predicting particle concentration. Consequently, this study was able to successfully determine that a CNN could simultaneously estimate a median particle size and concentration using ultrasonic backscatter data gathered on an "unknown" suspension.

1. Introduction

The difficulty to simultaneously characterise particle size and concentration in particle laden flows and processes *in situ* is prevalent across many industries [1–5]. Nuclear is one such industry, where many processes involved in decommissioning and waste treatment necessitate the handling of complex and dangerous suspensions and slurries [6–8]. It is not easy or practical when handling radioactive material in high volumes to sample, and consequently as part of ensuring safety and improving efficiency, a non-contacting characterisation technique is needed. Owing to the wide range of particle sizes and concentrations, and the dynamic changes these parameters undergo in different waste processing routes, a system which has the scope to operate effectively at both high and low concentrations of small and large particles is essential [9–11].

For appropriate technologies that may be operated remotely, laser-based particle characterisation systems and visual inspection methods are inappropriate, due to their inability to handle high solids loads and requirement for visual inspection ports. Alternatively, techniques such as electrical tomography systems may be used in concentrated systems

This article is part of a special issue entitled: IMFTF2024 published in Flow Measurement and Instrumentation.

* Corresponding author.
E-mail address: T.N.Hunter@leeds.ac.uk (T.N. Hunter).

https://doi.org/10.1016/j.flowmeasinst.2025.102926
Received 3 March 2025; Received in revised form 14 April 2025; Accepted 25 April 2025
Available online 28 April 2025

[12,13]. Nonetheless, while they are more widely applied in gas-liquid or liquid-liquid two phase systems [14], they can suffer from poor resolution with low concentrations of fine particles in solid-liquid systems. By contrast, acoustic backscatter systems (ABS) have already been demonstrated to characterise a wide variety of suspensions and slurries *in situ* with variable concentrations, for applications in engineering and environmental fields [15–21].

Acoustic backscatter operates at high frequency, in the megahertz range, where a transducer probe acts as both speaker and microphone, to produce an incident acoustic pulse and detect the scattering from features within the sample (in this case, particles within suspensions and slurries). The scattered signal is attenuated and dependent on particle concentration, particle size, temperature, and frequency used [22–24]. Variable concentration profiles, as well as particle sizes, in bulk samples have been identified previously, and concentration in pipe-flows has also been characterised, alongside flow regime identification and velocimetry, which provides an additional advantage over other techniques [1]. To determine the concentration of an unknown suspended particle system a calibration of the same suspended particle is needed, which also means that knowledge of the particle size distribution (PSD) is essential. The same can be said if identification of particle size is the aim, where a calibration of the same type of particle is needed from known concentrations. Recently, Pang et al., [25] reported new data processing techniques and a PSD inversion algorithm, using acoustic data gathered in a large diameter flows, to determine PSD estimates up to a mean absolute percentage error (MAPE) of 3.87 %–7.16 %, for a particle size range of 280–880 μm.

To alleviate this limitation, the use of Machine Learning (ML) is proposed, since ML is ideally suited for multi-variable minimisations [26]. ML works by training a digital machine with data gathered from a similar system, or set of systems, that allow the machine to optimise itself and predict the desired parameters from a target system. ML can be categorised into three main types; supervised, semi-supervised, and unsupervised, where each type corresponds to the detail of the labels of the training data used to train the machine [26]. This study utilises supervised learning, specifically artificial neural networks (ANN), which are structured in a similar way to the neurons within a human brain. Here, input data is fed into the ANN and a series of neuron layers are linked together such that the output provides the desired parameters. A convolutional neural network (CNN) is also deployed, as these deep learning architectures are ideally suited to image and pattern recognition [27,28]. CNNs can be defined as data filters which adaptively and automatically learn spatial hierarchies of features at low and high levels and are analogous to colour filters for image inspection [29].

ML has been used with ultrasound before to identify various processes and characterise fluid properties, such as whether a system is well mixed or not [30] and detection of fouling in flows [31]. A review by Bowler et al., [32] details numerous ways in which ultrasound and ML can be utilised together, focusing primarily on feature extraction, feature selection, algorithm choice, and hyperparameter selection, with suggestions on how to deploy both techniques. Dwinovantyo et al., [33] demonstrated that ANNs and acoustic Doppler current profile data can be used to classify zooplankton and suspended particles, with confidence values at $r > 0.95$ and offer predictions of zooplankton abundance and suspension concentration changes in dynamic environments with external physical variables. Gower et al., [34] investigated how both suspension concentration and particle size can be characterised from artificially generated backscatter data in the region close to the probe face, which although proving the applicability of ML and ABS for suspension characterisation, leaves questions on using ML with real data where variables may not be ideal.

This study aims to expand on this previous work, by using acoustic data gathered directly from well mixed suspensions rather than data generated artificially, allowing direct comparison to studies using the same suspended material and existing ultrasonic analytical techniques [15,35,36]. A custom-made calibration tank was used to achieve well-mixed suspensions with varied average particle size, distributions, and concentration, which were measured with a commercial instrument. The Thorne model [23] with the *G*-function method [37] was used to partially process the raw acoustic backscatter data before it was pre-processed and fed into machines for learning. Hyperparameter optimisations are presented as loss and mean-square-error (MSE) plots for the activation function of the ANN, as well as learning rate, filter number and filter width optimisations for the CNN. Acoustic scattering data was gathered on two further suspension systems, and predictions from each ANN and CNN model are reported relative to the true values. Although driven by the challenges of the nuclear sector, this work is applicable to any industry where simultaneous determination of concentration and size of particles in solid-liquid suspensions would be advantageous. Examples include dredging [38], slurry bubble column reactors for chemical and biochemical production [39], and mineral separation and classification, such as reflux classifiers [40].

2. Acoustic theory

2.1. Thorne model

The fundamental acoustic model, Eq. (1), as detailed by Thorne and Hanes [23], relates backscattered voltage, V, to distance from the transducer face, r, for a known mass concentration of suspended particles, M, with the assumption of single particle scattering, i.e. the acoustic signal reflected from one particle is not affected by its neighbouring particles. The pre-exponential expression describes the fraction of the wave that is reflected back at 180° to the transducer, with the transducer constant k_t, detailing the inbuilt gain of the system and probe characteristics. The particle backscatter constant, k_s, details the backscatter strength of the suspended particles. The nearfield correction factor, ψ, which tends to unity at the transition to the far-field can be taken as unity for all, given that only data in the far-field is analysed in this study.

$$V_{RMS} = \frac{k_t k_s}{\psi r} M^{0.5} e^{-2r(\alpha_w + \alpha_s)} \tag{1}$$

The limit of the near field is given as r_n, Eq. (2), where a_t is the active radius of the transducer and λ is the acoustic signal wavelength. A pre-factor of π is used here to allow results comparisons to Tonge et al., [35], and Downing et al., [41], although there is some dispute as to which pre-factor accurately describes the shape and limit of the near-field. The pre-factor chosen has been shown to produce results with errors close to zero at $z = 1$ [35].

$$r_n = \frac{\pi a_t^2}{\lambda} \tag{2}$$

The exponential expression in Eq. (1) describes the fraction of the wave that is attenuated by the fluid and suspended particles, with the constant for attenuation due to water at zero salinity, α_w (m^{-1}), from Ainslie and McColm [42], given as Eq. (3), which depends on the acoustic frequency, f (MHz), and temperature, T (°C).

$$\alpha_w = 0.05641 f^2 e^{-\left(\frac{T}{27}\right)} \tag{3}$$

The constant for attenuation due to suspended particles, α_s (m^{-1}), from Thorne and Hanes [23], is given as Eq. (4), and can be defined as the product of the mass concentration of suspended particles and the concentration-independent sediment attenuation coefficient (SAC), ξ, with respect to distance from the transducer face. When concentration is constant with respect to distance from the transducer face, Eq. (4) can be simplified to Eq. (5). The SAC can be defined by Eq. (6), where $(\chi_{ss}+\chi_{sv})$ is the dimensionless total normalised scattering cross section, ρ is the suspended particle density and a_s is the mean suspended particle radius.

$$\alpha_s = \left(\frac{1}{r}\right)\int_o^r \xi(r)M(r)dr \tag{4}$$

$$\alpha_s = M\xi \tag{5}$$

$$\xi = \frac{3(\chi_{ss}+\chi_{sv})}{4\rho\langle a_s\rangle} \tag{6}$$

The two terms within the total normalised scattering cross section describe the mechanisms of attenuation, in terms of the mean particle radius and acoustic wavenumber product, x, given by Eq. (7). Here, Eq. (8) and Eq. (9) also detail the heuristic expressions previously established by Betteridge, Thorne and Cooke [22] that describe attenuation due to scattering, χ_{ss}, for spherical glass beads, where single scattering is assumed.

$$x = ka_s = \frac{2\pi}{\lambda}a_s \tag{7}$$

$$\chi_{ss} = \frac{0.24\varphi x^4}{0.7+0.3x+2.1x^2-0.7x^3+0.3x^4} \tag{8}$$

$$\varphi = 1-0.4e^{-\left(\frac{x-5.5}{2.5}\right)^2} \tag{9}$$

When $x \ll 1$, the second mechanism, attenuation due to viscous losses, χ_{sv}, becomes most prominent and can be described by the model from Urick [24], detailed by Eq. (10) to Eq. (14). Here, ρ_0 is the density of the fluid surrounding the suspended particles, β describes the inverse of the viscous boundary layer thickness, where ω is the acoustic angular frequency, and ν_o is the kinematic viscosity of water.

$$\chi_{sv} = \frac{2}{3}x(g-1)^2\left[\frac{s}{s^2+(s+\delta)^2}\right] \tag{10}$$

$$g = \frac{\rho_s}{\rho_0} \tag{11}$$

$$s = \frac{9}{4\beta a_s}\left(1+\frac{1}{\beta a_s}\right) \tag{12}$$

$$\delta = \frac{1}{2}\left(1+\frac{9}{2\beta a_s}\right) \tag{13}$$

$$\beta = \sqrt{\frac{\omega}{2\nu_0}} \tag{14}$$

To illustrate how each mechanism affects the SAC as a function of particle radius, the SAC from each of the scattering and viscous models, as well as their totals, for 2 and 4 MHz are presented in Fig. 1. Attenuation is clearly much greater for 4 MHz compared to 2 MHz for both attenuating mechanisms, with the viscous mechanism more dominant at smaller particle radii, while the scattering mechanism is more dominant at larger particle radii. Given that particle sizes within sludges and slurries in the nuclear industry can vary from microns to hundreds of microns [6,43], it is important that both mechanisms are considered.

2.2. G-function

Rice et al., [37] devised a method that linearised Eq. (1) with respect to distance, by taking the natural logarithm of the product of the backscatter voltage, nearfield correction factor and distance. Labelled the G-function and shown in Eq. (15), this method has been utilised to quantify backscattering and attenuating properties of arbitrary suspensions [15,44].

$$G = \ln(\psi rV) = \ln(k_t k_s) + \frac{1}{2}lnM - 2r(\alpha_w+\alpha_s) \tag{15}$$

The partial derivative of the G-function can be taken, with respect to distance, to yield Eq. (16). If Eq. (5) remains true and is substituted for α_s, the partial derivative, with respect to concentration, of Eq. (16) can be taken yielding Eq. (17). This allows the SAC to be measured from taking the gradient of G plotted against distance over a range of well mixed homogeneous concentrations, ξ^m.

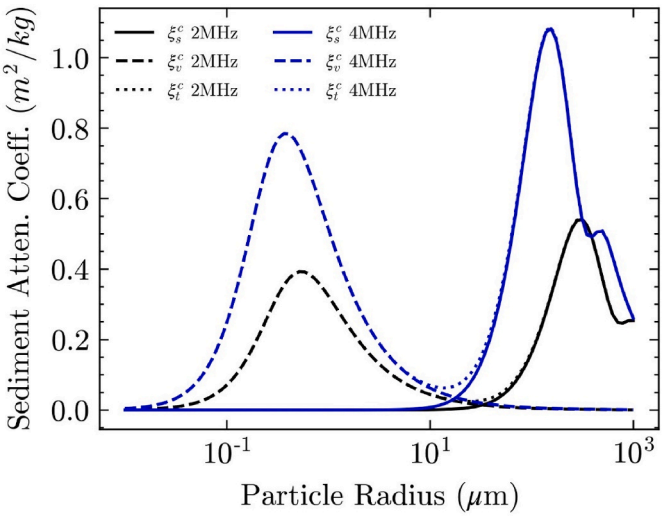

Fig. 1. Concentration independent sediment attenuation coefficient (SAC) against suspended particle radius calculated for 2 and 4 MHz from the scattering model [22], denoted by subscript s, and viscous [24] model, denoted by subscript v. Total SAC (sum) denoted by subscript t (superscript "c" in the legend denotes plots are calculated from the model and differentiates them from values measured from backscattered data).

$$\frac{\partial}{\partial r}[\ln(\psi rV)] = -2r(\alpha_w+\alpha_s) \tag{16}$$

$$\xi^m = -\frac{1}{2}\frac{\partial}{\partial M}\left[\frac{\partial}{\partial r}[\ln(\psi rV)]\right] = -\frac{1}{2}\frac{\partial^2 G}{\partial M \partial r} \tag{17}$$

This method requires knowledge of the system and the suspended particles to be characterised, such that a calibration using this method can be performed, therefore enabling unknown concentrations of the same particles to be determined.

3. Materials and methods

3.1. Materials

Three sizes of spherical silica glass beads; small (Honite 22), medium (Honite 16), and large (Honite 12), procured from Guyson International Ltd, UK were used as suspended particles. As ideal scatterers, heuristic expressions [22] and experimental methods [15,37] are well documented to determine their acoustic properties. Mixtures at 25:75, 50:50, and 75:25 wt%, of the small-to-medium, and medium-to-large sized glasses were made up to produce a total of nine systems with varying PSDs, that were used to train and test the ML codes. Two other systems at 33:67 wt% of small-to-medium and 67:33 wt% of medium-to-large sized glasses were also tested to provide data on "unknown" systems that the ML could make predictions from, such that comparisons between predictions and true values could be made. The high sphericity and morphology of the Honite material has been well documented by previous authors [15,35,45] and has shown only small shape deviation and surface defects. PSDs of all systems were verified using a Malvern Mastersizer 3000 (Malvern Instruments, UK). Here, log-normal distributions were fitted to the data to calculate the mean size and the coefficient of variation (CV), being the quotient of standard deviation and mean, and were used as labels for each system when training the machines.

For further work to test the limits of the CNN outside of the range of the training data, fine calcium carbonate 'Sturcal L' (Specialty Minerals Inc.) was used. Mastersizer measured particle size distribution and average sizes are reported within the Electronic Supplementary Materials (ESM), Fig. S1 and Table S1.

3.2. Experimental setup

A commercial ultrasonic velocity profiler (UVP), the UVP-DUO (Met-flow SA, Switzerland), was used for acoustic characterisation on all suspension systems. The UVP-DUO acts as both an ultrasonic acoustic backscatter system and an ultrasonic velocity profiler. The instrument consists of a central processing box and proprietary transducer probes connected via fixed cables. It allows for connections of up to four transducer probes at each frequency: 0.5, 1, 2, 4, and 5 MHz. Three 2 MHz probes and two 4 MHz probes, all with active radii of 5 mm, were used throughout this study to produce sufficient data for the machine learning. Fig. 2 presents a schematic detailing how UVP probes were mounted in mixed suspension off centre, using in a 0.8 m tall, 0.3 m diameter baffled cylindrical calibration tank. To ensure each suspension was well mixed and homogeneous, an over-head impeller mixer was mounted off centre, to minimise interference from reflections in the acoustic profiles. Additionally, a pipe loop with a Watson-Marlow 520s peristaltic pump was used to recirculate any settled material from the bottom of the conical bottomed tank, into the top portion of the suspension. Thus, a turbulent well mixed suspension is produced, where the recirculation flow was set only to mitigate any particle sedimentation segregation. Consequently, to minimise any acoustic interference from gas entrainment from the recirculation loop, the probes were mounted halfway down the depth of the tank. An image of the calibration tank during data collection is also shown within the ESM (Fig. S2).

Three sampling tubes were connected down the side of the tank, one at the depth of the probe faces, one at 100 mm below the probes and one at another 100 mm below that, to coincide with the main measurement region of the probes. Samples were taken simultaneously with a multi-headed pump and were dried in an oven to calculate concentration values for the six bulk concentrations of each individual glass size tested: 2.4, 14.1, 28.2, 42.4, 56.5 and 70.6 g/L. The bulk concentrations tested were achieved by top loading each glass by hand into 42.5 L of water in the tank at approximately 20 °C. After each addition of glass, several minutes were allowed for the suspension to homogenise before concertation samples were taken.

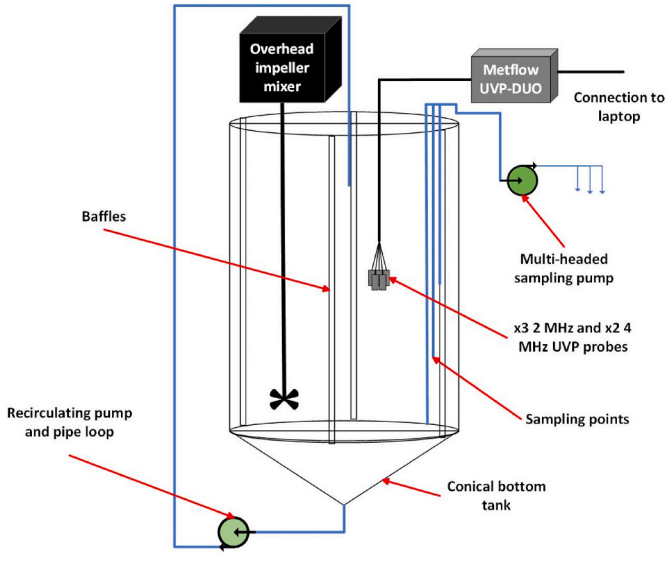

Fig. 2. Schematic of the recirculating calibration tank experimental setup with ultrasonic probe position (not to scale).

Acoustic data were then collected with the UVP, using the settings detailed within the ESM (Table S2). Consequently, between the nine glass particle systems, six concentrations and five acoustic probes, a total dataset of 270 averaged acoustic profiles were available for the ML code to learn from. Table 1 provides a breakdown of what each profile refers to.

3.3. Acoustic data processing

The backscatter data from the UVP for each profile outputs as a matrix of backscatter amplitudes, A, Eq. (18), in the shape n *x* 1024, where n is the number of channels and 1024 is the number of profiles, such that the outputs were 550 *x* 1024 and 1090 *x* 1024 sized arrays for 2 MHz and 4 MHz probes, respectively. All profiles for each channel were averaged by using the root-mean-square (RMS) to produce a single averaged backscatter amplitude profile, $E(r)$, Eq. (19).

$$A = \begin{bmatrix} 1,1 & \cdots & n,1 \\ \vdots & \ddots & \vdots \\ 1,1024 & \cdots & n,1024 \end{bmatrix} \tag{18}$$

$$E(r) = [\,1,\ RMS_1 \quad \ldots \quad n,\ RMS_n\,] \tag{19}$$

Eq. (20) was then used to convert the averaged raw amplitude backscatter data to backscatter voltage, $V(r)$, for analysis with the G-function method, using manufacturer supplied gain settings (Table 2). Due to the Doppler velocity (frequency shift measurement used by the UVP for velocity profiling) and the amplitude data being quantised into 14-bit data, each value could take one of 2^{14} values, N_d, thus this coefficient is included in the conversion, together with the gain function, $g(r)$, Eq. (21).

$$V(r) = \frac{5E(r)}{N_d g(r)} = \frac{(3.052 \times 10^{-4})E(r)}{g(r)} \tag{20}$$

$$g(r) = g_1\ exp\left[\ln\left(\frac{g_2}{g_1}\right) \cdot \frac{(r - r_1)}{(r_2 - r_1)}\right] \tag{21}$$

The gain, g, varies exponentially between the minimum and maximum measurement distances, r_1 and r_2 respectively, from the gain start to gain end values, g_1 and g_2, respectively. The associated absolute gain values to gain settings are detailed in Table 2 and were provided by Met-flow.

Table 1
Details of the 270 acoustic profiles used for the train-test dataset.

Particle ratio (wt. fraction)	Concentrations measured (g/L)	Probes used (MHz)	Total profiles
Small (100)	2.4, 14.1, 28.2, 42.4, 56.5, 70.6	2, 2, 2, 4, 4	30
Small:Medium (75:25)	2.4, 14.1, 28.2, 42.4, 56.5, 70.6	2, 2, 2, 4, 4	30
Small:Medium (50:50)	2.4, 14.1, 28.2, 42.4, 56.5, 70.6	2, 2, 2, 4, 4	30
Small:Medium (25:75)	2.4, 14.1, 28.2, 42.4, 56.5, 70.6	2, 2, 2, 4, 4	30
Medium (100)	2.4, 14.1, 28.2, 42.4, 56.5, 70.6	2, 2, 2, 4, 4	30
Medium:Large (75:25)	2.4, 14.1, 28.2, 42.4, 56.5, 70.6	2, 2, 2, 4, 4	30
Medium:Large (50:50)	2.4, 14.1, 28.2, 42.4, 56.5, 70.6	2, 2, 2, 4, 4	30
Medium:Large (25:75)	2.4, 14.1, 28.2, 42.4, 56.5, 70.6	2, 2, 2, 4, 4	30
Large (100)	2.4, 14.1, 28.2, 42.4, 56.5, 70.6	2, 2, 2, 4, 4	30
Cumulative Total			**270**

Table 2
UVP-DUO gain settings.

Setting	3	4	5	6	7	8	9
Absolute	0.91	1.76	3.41	6.67	15.00	25.00	60.00
Log. (dB)	−0.8	4.9	10.7	16.5	23.5	28.0	35.6

4. Machine learning methods

The key variables of any ML structure can be defined as; loss function, number of layers, number of neurons per layer, activation function, optimisation function, learning rate, and in the case of CNNs, filter dimensions and filter number. The loss function can be defined as the difference between the output value and the true value and in this study is taken using the mean squared error function [26]. The number of layers, number of neurons in each layer, and activation function were determined in this study through consideration of existing ML architectures for common applications and iteratively improved [26,32]. The activation function can be defined as a mathematical function that calculates the output of a neuron from its inputs and weights, for all layers in both the ANN and CNN. In this study, the ReLU (Rectified Linear Unit) function was used and is expressed as the non-negative part of its argument [46].

The hyperparameters are variables that are actively varied and optimised to tailor the neural networks to find the best solutions. The optimisation function can be defined as the mathematical operation to determine what change in the weights between neurons should be made to reduce the loss function. A number of different optimisers were trialled in this study, and for more detail on the expanding range of optimisers available, please see the review by Nwankpa [47]. The learning rate can be defined as how small or large the changes to these weights are; too high a learning rate and the loss function will tend to diverge while too low and the training will be too computational expensive and may only find a local minima rather than the system minima in the loss function [48]. A range of fixed learning rates were tested in this study, while there are multiple approaches to determining the ideal learning rate with literature still uncertain as to which is best, as are detailed in Montavon et al., [49] and Nwankpa [47].

The filter dimensions can be defined as the proportion of the training data that is fed into the filter kernel in the CNN with each pass. In this study, the training data only has one dimension so it can be described with a single number, filter width. Filter number can be defined as how many filter kernels are used on the filter dimensions. In this study, several variations were tested, corresponding to computer bit formatting numbers. All pre-processing, ML architecture, testing, training, and prediction operations were conducted using the Python programming language in VS Code. The Tensorflow keras library was utilised for the construction of both the ANN and CNN machines with Scikit learn used for the test-train-run operations and measurement of effectiveness of the predictions by the r-squared function, which is common practice for ML applications [49].

4.1. Pre-processing

The raw *G*-function data were initially loaded and transformed by isolating the most important segments of the data, omitting a small section very close to the probe face, where the acoustic wave is in the nearfield, and a section at the end of each profile that corresponds to where the return signal is below the noise floor of the instrument. These segments of the *G*-function were extracted based on predetermined frequency-dependent start and end points, before being uniformly resampled to a fixed length of 999 data points through linear interpolation. The original probe frequency value, which was appended to each interpolated signal, was subsequently normalised into a binary indicator such that a frequency of 4.0 MHz was represented as 1.0 and a frequency of 2.0 MHz was converted to 0.0. These fully pre-processed data were then exported. Subsequently, the training data were loaded into the ML training algorithm, with the first three columns designated as predicted variables and the remaining columns as input features. The input and prediction data were then normalised using a min-max scaling approach, ensuring that each variable was scaled consistently, also as common practice in ML techniques [49].

4.2. ANN and CNN architecture

Two neural network architectures were iteratively designed and optimised to predict the PSD, as well as the concentration simultaneously for each pre-processed *G*-function. A detailed layer-wise overview is provided in Table 3, and as diagrams in the ESM (Fig. S3), which indicates the parameters that were varied to optimise the performance of the technique. In both cases, all layers are fully connected.

The ANN comprises of five hidden layers in all cases, with the number of neurons progressively decreasing in deeper layers. Each neuron employs the ReLU activation function, while the output layer consists of three neurons corresponding to the normalised median particle diameter, CV, and concentration. In contrast, the CNN includes an additional one-dimensional convolution layer, which applies a variable number of filters of a specific width to the input data for feature extraction. This layer processes the normalised *G*-function signal by iteratively sliding each filter along the input array, performing element-wise multiplications with overlapping values, and summing the results to produce an output. This operation is repeated across the entire signal, generating feature maps that are propagated through subsequent layers. The flattened layer then reshapes the convolution layer's output into a one-dimensional tensor, which is processed similarly to the ANN's structure. Both networks were trained for 500 epochs using various optimisers to minimise the root-mean-square error as the loss function. Training was conducted with a batch size of 32 and a train-test split of 70:30 for validation purposes.

4.3. Hyperparameter optimisation

Hyperparameter optimisation was performed to enhance the predictive accuracy and generalisation capability of both the ANN and CNN models used in this study. The key hyperparameters considered were the optimisation function, as well as the learning rate, filter number and filter width for the CNN.

In particular, the optimiser plays a crucial role in updating network weights and controlling the rate of convergence (as well as the final accuracy) during training. Several optimisers were evaluated, including Stochastic Gradient Descent (SGD), Adam, Nadam and RMSprop. SGD is an optimisation algorithm which updates weights by computing the gradient of the loss function. While simple and computationally efficient, it often converges slowly and is sensitive to learning rate selection. Adam is a more adaptive learning rate optimiser which combines momentum in convergence and scaling of gradients using both first and

Table 3
ANN and CNN architecture, where parameters indicated in bold were found to be optimal based on the listed variations and used in the final ML model.

ANN		CNN	
Layer	Hyperparameters	Layer	Hyperparameters
Input	$N = 1000$	Input	$N = 1000$
Flatten	–	Conv1D	$FN = 32, \mathbf{64}, 128$ $FW = \mathbf{5}, 10, 20$
Dense	$N = 1024$	Flatten	–
Dense	$N = 512$	Dense	$N = 1024$
Dense	$N = 256$	Dense	$N = 512$
Dense	$N = 128$	Dense	$N = 256$
Dense	$N = 32$	Dense	$N = 128$
Output	$N = 3$	Dense	$N = 32$
		Output	$N = 3$

second moment estimates. It is well-suited for deeper networks and generally provides faster convergence than SGD. RMSprop is similar to Adam but lacks the momentum component. It is more effective for non-stationary objectives and stabilising learning in deep networks. Finally, Nadam is a variation of Adam which incorporates Nesterov momentum. This metric anticipates the future direction of the gradient and results in faster convergence and reduced loss oscillations.

5. Results and discussion

5.1. Materials

The log-normal volume size distributions of all nine training systems are presented in Fig. 3, with median, mean, and standard deviation (St. Dev.) values calculated from the log-normal fit, along with CVs for all nine systems which are reported in Table 4.

The three monodisperse systems display the tightest distributions, as is reinforced by the corresponding CV values. The 25:75 wt% mixes have wider distributions relative to their monodisperse glasses, where each system's median is shifted to the dominant monodisperse glass within each and, as such, the distributions are broadened, and their corresponding CV values are larger. The 50:50 wt% mixes show an even greater spread in distribution, again with broadened plots with the largest CV values reported. While the median of the small:medium 50:50 wt% distribution is almost equidistant between the two monodisperse glasses, the median of the medium:large 50:50 wt% system is closer to the medium sized glass. This is likely due to the fines playing a more significant role at these larger particle sizes, such that the sample tested contained a slightly elevated proportion of the medium sized glass relative to the large sized glass. However, given the median still sits between the two 25:75 wt% mixes of that system, it still serves the purpose of providing a training system with particle characteristics between the others. These systems provided a range of median particle sizes and CVs such that the acoustic profiles gathered on them would provide adequate training data for the machines.

Table 4
Median, mean, SD, and CV values for all nine training systems. Underlined values indicate the labels used, in conjunction with the concentrations, for the training of the ANN and CNN machines.

Particle ratio (wt. fraction)	Median (μm)	Mean (μm)	St. Dev. (μm)	CV
Small (100)	35.7	37.1	10.4	0.281
Small:Medium (75:25)	42.0	45.6	19.3	0.424
Small:Medium (50:50)	69.8	82.7	52.6	0.636
Small:Medium (25:75)	80.3	88.6	41.4	0.467
Medium (100)	81.6	83.0	15.6	0.187
Medium:Large (75:25)	105	114	50.2	0.439
Medium:Large (50:50)	134	155	90.3	0.584
Medium:Large (25:75)	205	226	103	0.456
Large (100)	203	206	39.8	0.193

Fig. 4 shows the log-normal volume size distributions of the "unknown" systems used to test the machines after training was complete. These mixes were chosen as they offered variation in median size and CV either side of the median, of the medium size monodisperse glass system. Thus, the ML was used to interpolate within the parameter space, rather than extrapolate beyond for all three of the parameters when making predictions on "unknown" data. Table 5 details median, mean, and standard deviation (SD) values calculated from the log-normal fit, along with CVs for both "unknown" systems. Here, the small:medium 33:67 wt % median and CV values are between the medium 100 wt% and the small:medium 25:75 wt% values, and the medium:large 67:33 wt% median and CV values are between the medium 100 wt% and the medium:large 75:25 wt%. As such, they provide two systems that offer different values the machines need to predict other than those they were trained on. When considering the median values with reference to the acoustic analytical models presented in Fig. 1, these glass systems are all

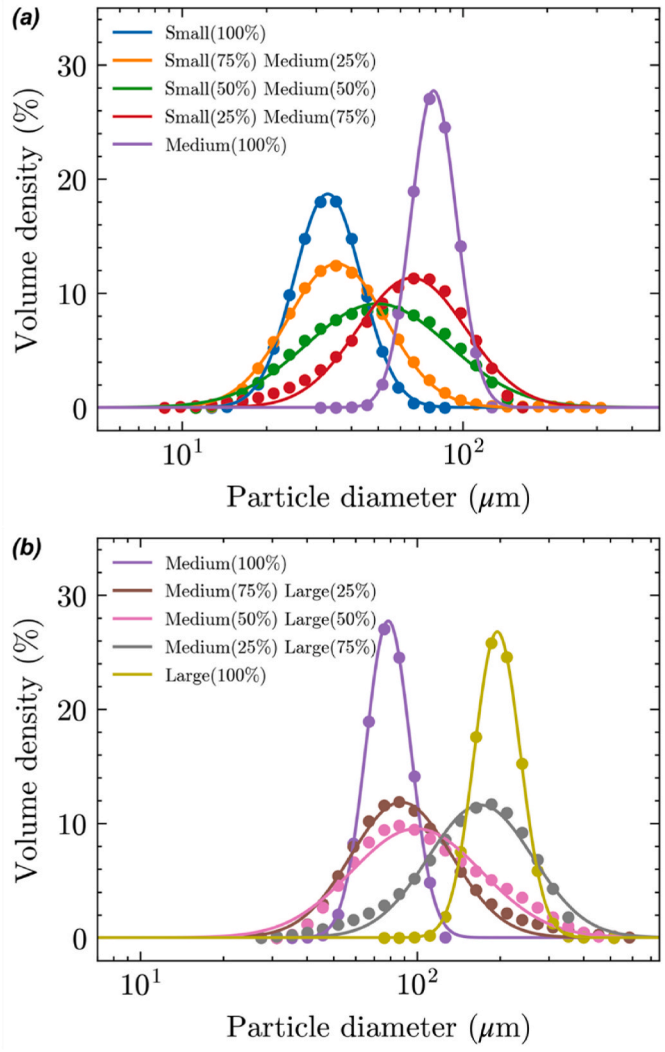

Fig. 3. Particle size distributions of (a) small:medium, and (b) medium:large, spherical silica glass bead systems from a log-normal fit of data gathered with a Malvern Mastersizer 3000.

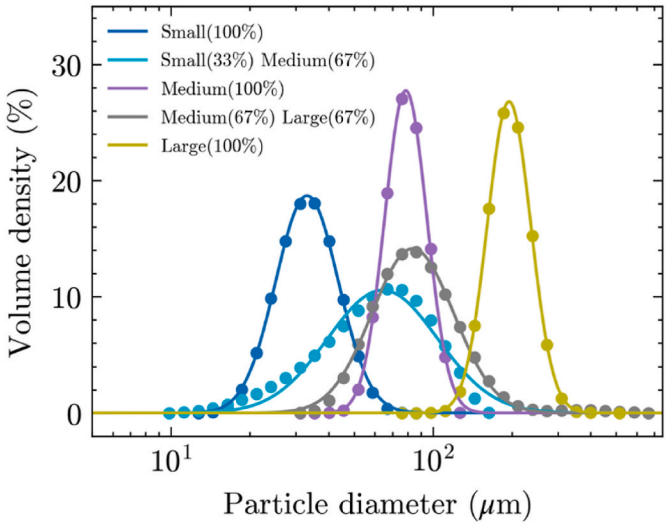

Fig. 4. Particle size distributions of "unknown" spherical silica glass bead systems from a log-normal fit of data gathered with a Malvern Mastersizer 3000.

Table 5
Median, mean, standard deviation (St. Dev.), and coefficient of variation (CV) values for "unknown" spherical silica glass bead systems.

Particle ratio (wt. fraction)	Median (μm)	Mean (μm)	St. Dev. (μm)	CV
Small:Medium (33:67)	81.1	91.2	46.7	0.512
Medium:Large (67:33)	95.3	101	37.8	0.371

expected to be dominated by the scattering attenuation mechanism and directly proportional to particle size [35].

Concentration verification of the monodisperse glass systems in the calibration tank is presented in Fig. 5 as box plots, where each box shows the interquartile range (IQR) of the three measurements taken (top, middle and bottom), and the line in the middle of each box shows the median and the vertical bars denote x1.5 the IQR from the respective quartile marker. The IQR of all three systems increases as concentration increases, because the mixing energy needed to maintain a homogeneous suspension is not being fully met as more particles are added. This issue is most obvious in the large glass system, due to the larger mass of the glass beads and their increased tendency to settle, which results in some concentration variation. Yet, due to the large number of ultrasonic profiles averaged (1024), the small range in measured concentration is not thought to have caused significant issues, especially given that previous authors have found good agreement between measured and modelled values when using similar materials and experimental set-ups for acoustic calibration [15,35,44].

5.2. Optimiser and ANN/CNN comparison

Fig. 6 demonstrates the respective reduction in loss and MSE for the ANN while varying the optimiser and comparing the training and testing accuracy. In both cases, the plots indicate that Nadam consistently outperformed the other optimisers in terms of convergence speed and accuracy, reducing oscillations and improving generalisation, and with deviation indicative of overfitting taking place beyond around 100 epochs. Nadam was also found to be the most effective for the CNN, as demonstrated in Fig. 7, as it provided the lowest loss and mean square error across both models, ensuring faster convergence and improved generalisation. That said, overfitting was exhibited earlier at around 80 epochs.

Analysing both Figs. 6 and 7 illustrates the performance comparison

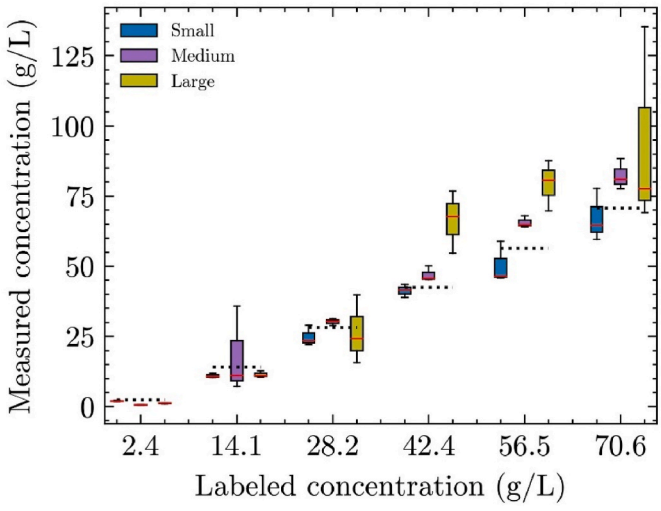

Fig. 5. Concentration verification, where boxes show the respective interquartile range of the three measurements taken for each glass at each concentration, the middle line in each box denotes the median and vertical bars denote x1.5 the interquartile range from the respective quartile marker. Dashed lines show labelled concentration relative to the *y* axis.

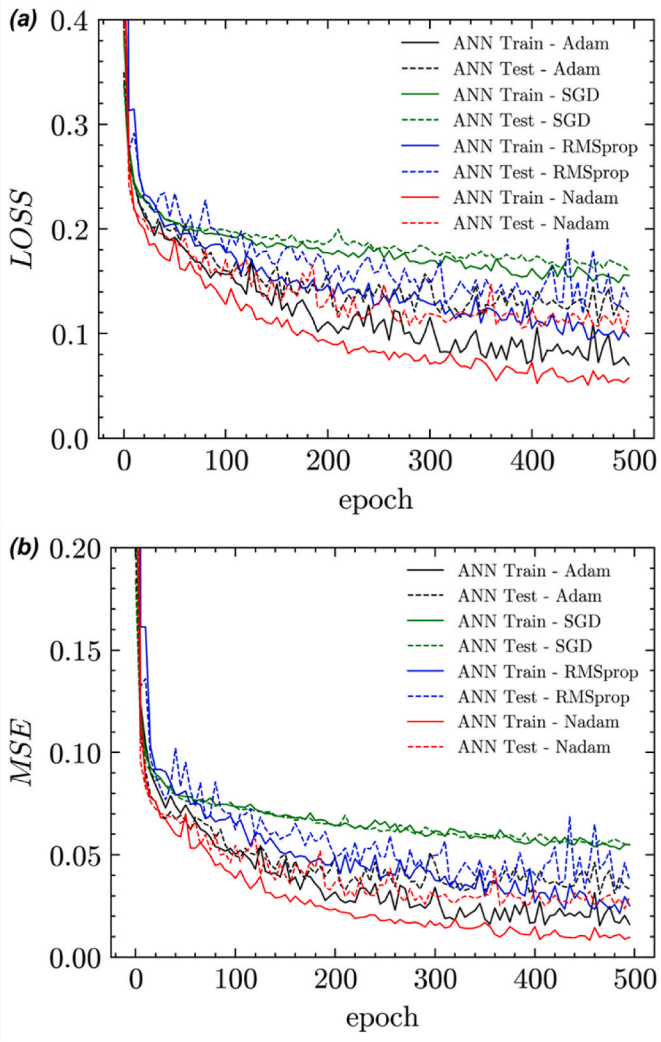

Fig. 6. (a) Loss and (b) MSE curves from comparison of optimiser for ANN.

between ANN and CNN models across different optimisers. It is demonstrated that the CNN consistently outperformed the ANN, in terms of lower loss values and MSE across most optimiser configurations. This is likely because the convolutional layer in a CNN enables more efficient feature extraction and pattern detection from the acoustic data, allowing for improved generalisation to "unknown" data. Moreover, the CNN demonstrated superior stability during training, as observed in the smoother convergence trends in Fig. 7. This difference indicates that the CNN was less prone to overfitting and handled variations in data more effectively. The ability of the CNN to learn patterns in the feature data makes it a more suitable model for predicting particle size distribution and concentration from ultrasonic backscatter data, and hence was chosen for the remaining optimisations.

5.3. Learning rate, filter number and filter width with the CNN

Learning rate is also an important hyperparameter that controls the step size of weight updates during the training algorithm. Fig. 8 presents the performance of CNN models trained with different learning rates, where 0.0001, 0.001, and 0.01 were tested. A learning rate of 0.001 provided the best trade-off between stability and convergence speed. The lower learning rate led to slower convergence, while higher learning rates resulted in more erratic updates, characterised by the irregular spikes in accuracy in the loss and MSE plots, and failed to achieve an optimal loss reduction when compared to the others. The selected

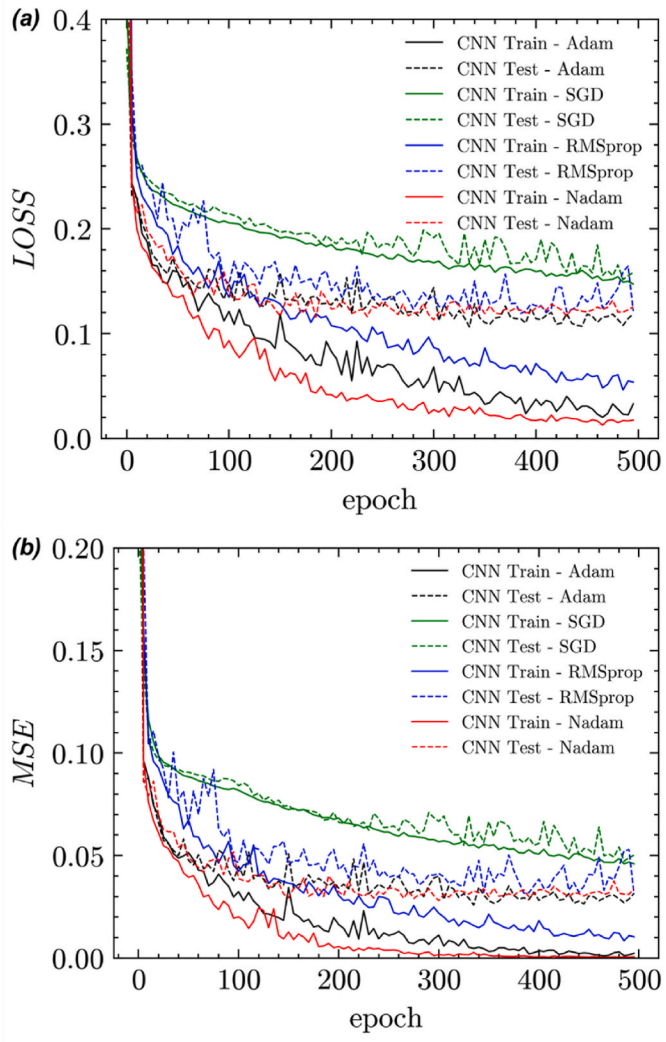

Fig. 7. (a) Loss and (b) MSE curves from comparison of optimiser for CNN.

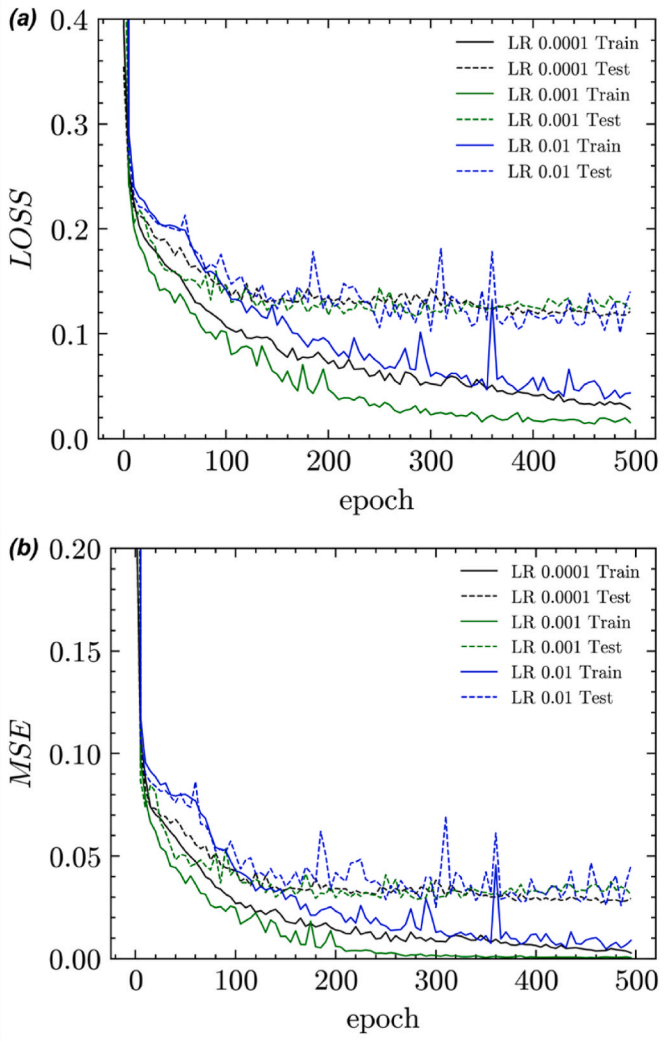

Fig. 8. (a) Loss and (b) MSE curves from learning rate optimisation for CNN.

learning rate of 0.001 ensured smooth and efficient training, minimising the risk of overfitting while achieving a lower MSE.

The CNN architecture included a convolutional layer responsible for feature extraction from the *G*-function training data. The number of filters directly affects the network's capacity to capture meaningful patterns within the data, which was shown to be important due to the improvements in accuracy when switching from the ANN to the CNN. A higher number of filters allows the network to detect more complex features but increases computational cost and increases the risk of overfitting. Conversely, too few filters may lead to insufficient feature extraction, reducing predictive accuracy. Fig. 9 presents the results of optimisation tests for the CNN conducted with 32, 64, and 128 filters and the evaluations were again based on loss values and MSE trends.

The comparisons indicated that 64 filters provided the best balance between performance and computational efficiency, however, the results further indicated that 128 filters provided marginally improved MSE and better accuracy, ensuring the most effective feature extraction. In contrast, the 32 and 64 filters resulted in comparatively higher RMS, suggesting inadequate feature representation. Based on the above, 128 filters were selected as the optimal configuration, allowing the CNN to achieve maximum accuracy.

The filter width determines the receptive field of the convolution operation, defining how much of the input data each filter considers at a time. A larger filter width allows the network to capture broader spatial patterns, while a smaller filter width focuses on finer details. Achieving a balance between the two is essential to ensure the CNN captures the most relevant patterns without losing important resolution detail. Fig. 10 illustrates the performance of CNN models trained with filter widths of 5, 10, and 20. The optimal filter width was determined to be 5, as it provided the best trade-off between feature generalisation and resolution, resulting in the lowest MSE and best predictive performance.

5.4. *Predictions for "unknown" suspension systems*

In the previous sections, we demonstrated that the ML technique offered strong predictive capabilities when trained on well-characterised suspension systems. In this section, the trained models are evaluated on "unknown" suspension systems, distinct from those used during training, to determine their ability to infer PSD and concentration without prior exposure to the specific compositions. This test serves to further validate the robustness and adaptability of the ML approach for real-world applications, where suspensions may exhibit significant variability in their physical properties.

Fig. 11 presents the predicted median particle sizes for the "unknown" suspension systems using both the ANN and CNN models, compared to the true values obtained through experimental validation. While the ANN demonstrates reasonable predictive capability, its estimations exhibit noticeable deviations from the true values, particularly for systems with larger particles. In contrast, the CNN significantly improves predictive accuracy, with median values closely aligned with the

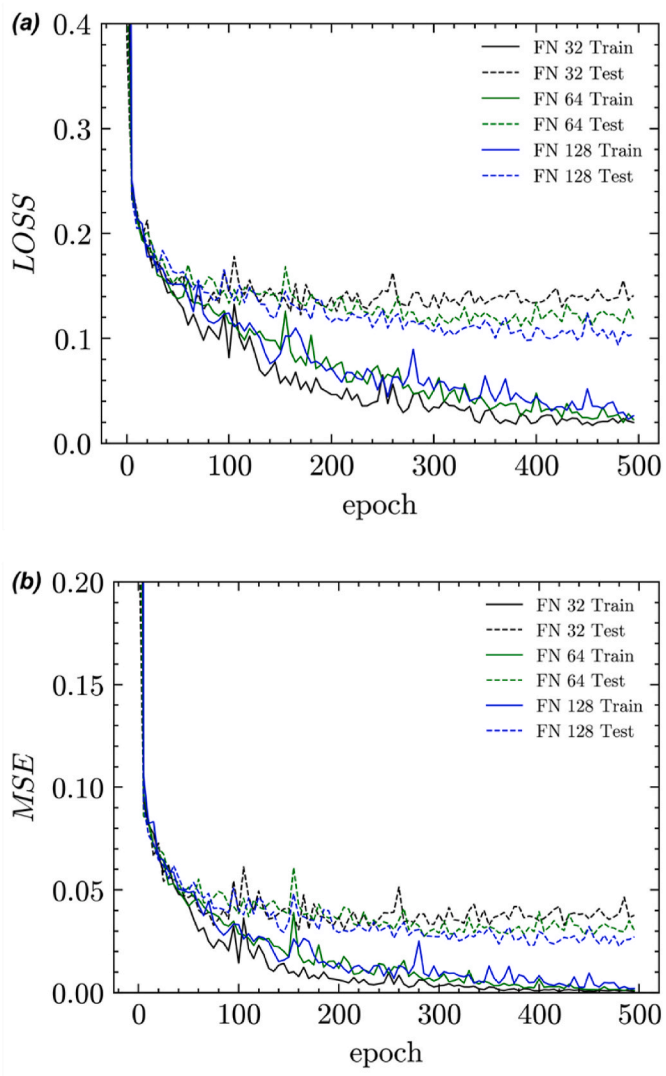

Fig. 9. (a) Loss and (b) MSE curves from filter number optimisation for CNN.

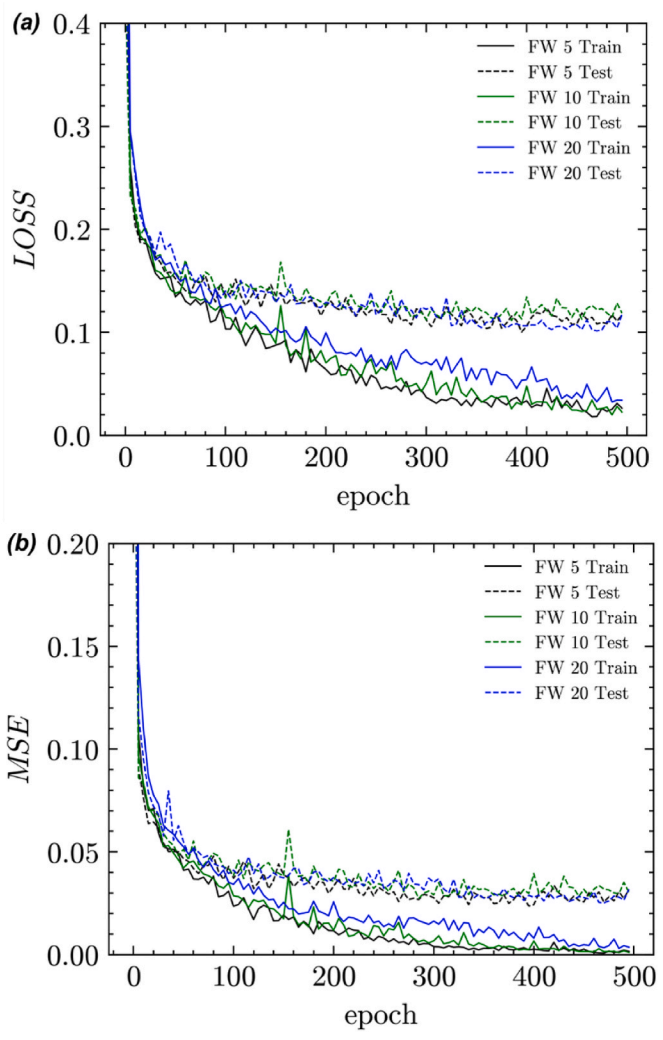

Fig. 10. (a) Loss and (b) MSE curves from filter width optimisation for CNN.

actual particle sizes across all tested systems. This enhancement can be attributed to the CNN's ability to extract and learn spatial features from the ultrasonic backscatter data more effectively, allowing for better generalisation beyond the training dataset [50]. The reduced interquartile ranges in CNN predictions also highlight its superior capability in capturing complex patterns in acoustic data, reinforcing its suitability for robust and reliable median particle diameter characterisation in "unknown" systems. In this case, the interquartile range is lower for the larger particles, though the full range is higher. This difference indicates that the CNN more often predicts diameters close to the true value for larger particles. However, some outliers may be present, likely dependent upon the current state of mixing within the system, and the high attenuation of larger particles that may dominate the acoustic response results in increased variability in some instances.

Fig. 12 illustrates the predicted CV for the "unknown" suspension systems using both the ANN and CNN models, compared to the true values. Unlike the improvements seen in median particle size predictions, the CV predictions remain relatively poorer for both models, with slight improvements in estimations when the CNN is used. Nevertheless, the CNN does not show the same level of refinement here as it does for median particle size, indicating that the network struggles to capture the full complexity of PSD variability from the acoustic data. This difference suggests that the current feature extraction process may not adequately represent the spread of particle sizes, or that additional training data covering a broader range of distributions may be required. Further refinement of the model architecture, or the inclusion of additional statistical features in training, may be necessary to improve predictive accuracy for this parameter.

Finally, Fig. 13 compares the predicted suspension concentrations from the ANN and CNN models against the true values. While the ANN exhibits considerable error and variability in its predictions, particularly for the highest concentrations, the CNN demonstrates a very strong improvement, producing estimates that closely align with the experimentally measured concentrations across all tested systems. This significant enhancement clearly demonstrates the CNN's superior ability to discern meaningful patterns in the acoustic data, effectively distinguishing concentration-dependent variations. It is likely that the convolutional layer allows the model to identify patterns from the acoustic signals, leading to more reliable and generalisable predictions. Fig. 13 also demonstrates an improvement on the established analytical method using the *G*-function approach, which has previously struggled to deal with high attenuating systems at high concentrations [35]. The CNN's success in both the median particle diameter and suspension concentration estimations highlights its potential for real-world applications, such as in nuclear decommissioning, where accurate, non-contact measurement of suspension properties is essential [6].

To test the limits of the ML model's predictive capabilities, the fine calcium carbonate particles (d_{50} ~15 μm) were also used as an "unknown" suspension, outside of the particle size range. This material also

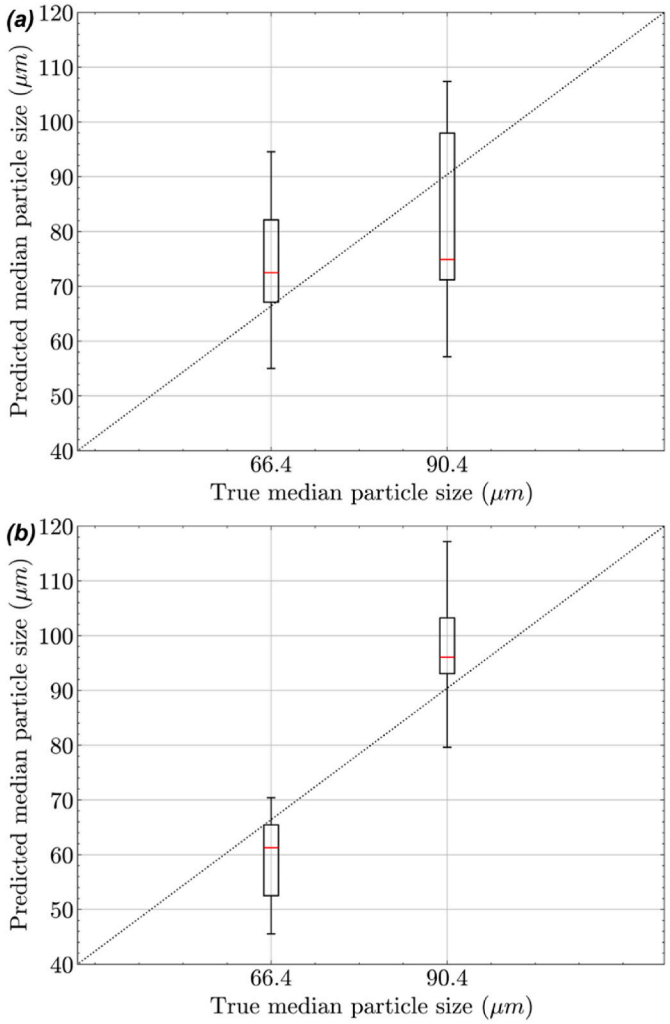

Fig. 11. Box plot predictions of average particle size made by the *(a)* ANN and *(b)* CNN from ultrasonic backscatter data, and true values for each "unknown" system. Boxes show the respective interquartile range of the 18 measurements (six concentrations from three 2 MHz probes and two 4 MHz probes) taken for each glass system, the middle line in each box denotes the median and vertical bars denote x1.5 the interquartile range from the respective quartile marker.

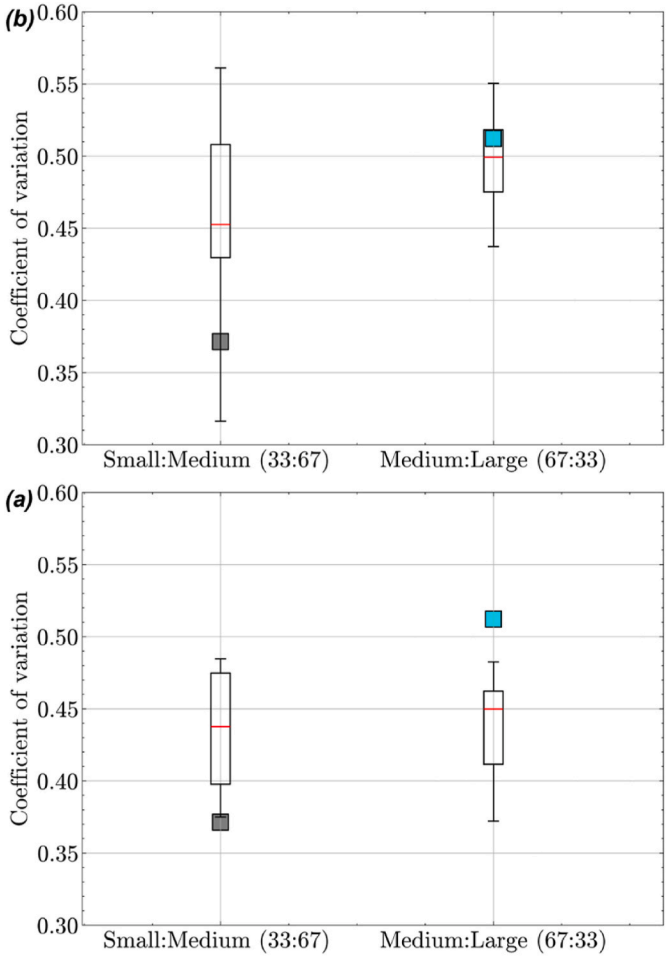

Fig. 12. Box plot predictions for coefficient of variation of the PSDs made by the *(a)* ANN and *(b)* CNN from ultrasonic backscatter data, and true values for each "unknown" system. Boxes show the respective interquartile range of the 18 measurements (six concentrations from three 2 MHz probes and two 4 MHz probes) taken for each glass system, the middle line in each box denotes the median and vertical bars denote x1.5 the interquartile range from the respective quartile marker.

has significantly different morphology and density to the glass, and as these variables also affect the acoustic backscatter response, prediction of desired suspension parameters proved a challenge to the ML models. A box plot of the concentration predictions against true values, with an inset table detailing the median, upper- and lower-interquartile range for median particle size and CV for the calcium carbonate suspension are provided within the ESM (Fig. S4).

Particle size predictions were significantly overestimated. It is assumed this largely stems from the fact that the ML model had been trained on suspensions where the scattering attenuation mechanism is dominant, hence, higher attenuation correlates to larger particles, as can be seen in Fig. 1. However, for the calcium carbonate system, the true particle size is lower, and within the region where viscous attenuation mechanism also becomes important where total attenuation increases as particle size decreases. For smaller micron sized particles, the complexity of competing viscous and scattering attenuation demonstrates a limitation of the ML model more generally. If relationships between variables that the ML model has not been trained on, it struggles to predict them from "unknown" data sets. Nevertheless, concentration predictions (Fig. S4) were reasonable for the lowest concentrations tested, but over predicted at moderate to high particle levels. It is thought that this result may be from the difficulty resolving weak signals where high interparticle scattering is present, which also increases overall attenuation. It is noted that in previous work with flocculated calcium carbonate, Tong et al., [51] showed similar over predictions when using analytical attenuation coefficient ratios. In that case, predicted concentrations trended towards infinity at high particle levels. Here, the ML model provides a much more stable estimate, but more research is required into how increasing the range of the training data into the viscous dominated regime may further improve the accuracy of size and concentration predictions.

6. Conclusions

The present work aimed to demonstrate the application of ANNs and CNNs to characterise particle suspensions using pre-processed ultrasonic backscatter data. A range of well-mixed silica glass bead suspensions with varying particle sizes, distributions, and concentrations were used to generate training and validation datasets. The data were pre-processed and analysed using ML models, and optimisation of a range of hyperparameters was conducted to improve predictive accuracy. The key findings indicate that CNNs outperform ANNs in predicting median particle size and concentration from ultrasonic backscatter data. CNNs were shown to have effectively learned spatial patterns within the data,

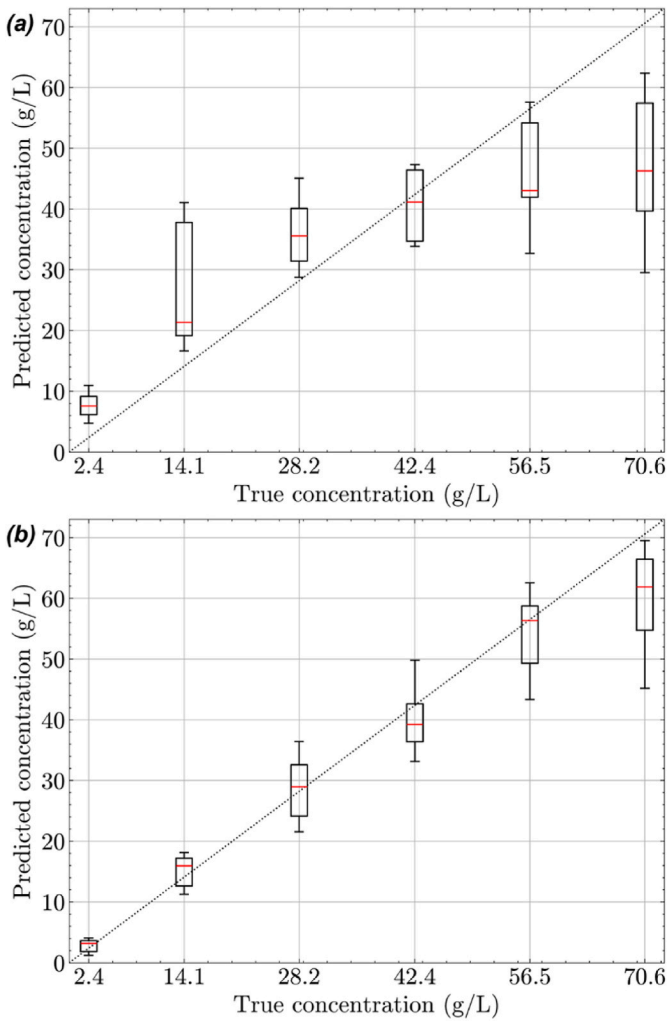

Fig. 13. Box plot predictions of concentration made by the *(a)* ANN and *(b)* CNN from ultrasonic backscatter data, and true values for each "unknown" system. Boxes show the respective interquartile range of the 12 measurements taken for each concentration across two glass systems for three 2 MHz probes and two 4 MHz probes, the middle line in each box denotes the median and vertical bars denote x1.5 the interquartile range from the respective quartile marker.

leading to more accurate estimations, particularly for lower particle concentrations and particle sizes. Throughout, the CNN models demonstrated superior generalisation capabilities, also achieving closer alignment with true values in "unknown" particle systems. In contrast, ANNs exhibited higher error rates and inconsistencies, particularly at larger particle sizes and higher concentrations. Despite these advancements, the models were less effective at predicting the CV of the PSDs. This limitation suggests that additional feature extraction techniques or expanded training datasets incorporating a wider range of PSDs may be necessary to improve the predictive accuracy. Future work should explore alternative ML architectures, hybrid models, additional input features or larger training datasets to enhance prediction reliability across all suspension parameters.

A major novelty of this study is the ability to predict both particle size and concentration simultaneously using a single ML model. This has never, to the authors' knowledge, been achieved before with ultrasonic backscatter data, as previous studies have typically focused on either particle size or concentration independently, with one used to obtain the other. From the presented results, the signal data generated from the acoustic technique encodes information surrounding both parameters, which implies that there is some further theoretical way to obtain both sets of information simultaneously. Judging by the improvements offered by the CNN technique, patterns within the signal play a more important role in the concentration calculation, which exhibited significant improvements. The accuracy of the technique is shown here to generalise well to "unseen" data within the parameter ranges trained upon initially. Further exploration into generalisation of the technique outside of the parameter ranges (at a different particle size and density) indicated poorer agreement. Here, it is thought that competing viscous attenation is a further complication that requires additional training data. Nevertheless, the integration of both parameters within a single predictive framework represents a significant advancement, offering a more comprehensive characterisation method that enhances the accuracy and efficiency of suspension analysis across multiple industrial sectors. The impact and usefulness of this work is significant for both generic industrial and nuclear decommissioning applications which require non-invasive, real-time suspension characterisation. In industries such as chemical processing, pharmaceuticals, and mining, accurate *in situ* measurement of particle size and concentration is crucial for process optimisation and quality control. In the nuclear industry, where handling and sampling of radioactive suspensions pose significant challenges, the use of ML-enhanced acoustic techniques offers a safer and more efficient alternative to conventional characterisation methods. By reducing reliance on manual sampling and offline analysis, this approach can improve operational efficiency and safety in nuclear waste management, decommissioning, and slurry monitoring applications. Overall, this study demonstrates the potential of ML techniques in advancing acoustic backscatter characterisation methods and sets the foundation for further research into refining predictive models for broader industrial and scientific applications.

CRediT authorship contribution statement

Joseph J. Hartley: Writing – original draft, Software, Methodology, Investigation, Formal analysis, Data curation, Conceptualization. **Lee F. Mortimer:** Writing – original draft, Software, Methodology, Investigation, Formal analysis, Data curation. **Jeffrey Peakall:** Writing – review & editing, Supervision, Resources, Funding acquisition, Conceptualization. **Richard A. Bourne:** Writing – review & editing, Supervision, Resources, Conceptualization. **Jonathan M. Dodds:** Writing – review & editing, Supervision, Resources, Project administration. **Martyn G. Barnes:** Writing – review & editing, Supervision, Funding acquisition, Conceptualization. **Michael Fairweather:** Writing – review & editing, Supervision, Resources, Funding acquisition. **Timothy N. Hunter:** Writing – review & editing, Supervision, Resources, Project administration, Methodology, Investigation, Funding acquisition, Conceptualization.

Declaration of competing interest

The authors declare the following financial interests/personal relationships which may be considered as potential competing interests: Timothy Hunter reports financial support was provided by Engineering and Physical Sciences Research Council. Joseph Hartley reports financial support was provided by Engineering and Physical Sciences Research Council. Michael Fairweather reports financial support was provided by Engineering and Physical Sciences Research Council. If there are other authors, they declare that they have no known competing financial interests or personal relationships that could have appeared to influence the work reported in this paper.

Acknowledgements

The authors acknowledge the University of Leeds, Sellafield Ltd and the Engineering and Physical Sciences Research Council (EPSRC) UK for funding this research through the TRANSCEND (Transformative Science and Engineering for Nuclear Decommissioning) consortium (Grant No.

EP/S01019X/1). The UK National Nuclear Laboratory (UKNNL) is thanked for project management. Thanks are also given to Christopher Bulman for laboratory assistance, and to Met-Flow Ltd. for instrument support.

Appendix A. Supplementary data

Supplementary data to this article can be found online at https://doi.org/10.1016/j.flowmeasinst.2025.102926.

Data availability

Data will be made available on request.

References

[1] D.M. Scott, Recent advances in in-process characterization of suspensions and slurries, Powder Technol. 399 (2022) 117159.
[2] A. Vergne, C. Berni, J. Le Coz, F. Tencé, Acoustic backscatter and attenuation due to river fine sediments: experimental evaluation of models and inversion methods, Water Resour. Res. 57 (9) (2021) e2021WR02958.
[3] S. Hoche, M.A. Hussein, T. Becker, Ultrasound-based density determination via buffer rod techniques: a review, JSSS 2 (2) (2013) 103–125.
[4] L. Liang, Y. Peng, J. Tan, G. Xie, A review of the modern characterization techniques for flocs in mineral processing, Miner. Eng. 84 (2015) 130–144.
[5] M. Wang (Ed.), Industrial Tomography: Systems and Applications, 2015. Cambridge.
[6] C.R. Gregson, D.T. Goddard, M.J. Sarsfield, R.J. Taylor, Combined electron microscopy and vibrational spectroscopy study of corroded Magnox sludge from a legacy spent nuclear fuel storage pond, J. Nucl. Mater. 412 (1) (2011) 145–156.
[7] R. Burrows, S. Harris, N.P.C. Stevens, Corrosion Electrochemistry of fuel element materials in pond storage conditions, Chem. Eng. Res. Des. 83 (7) (2005) 887–892.
[8] J.J. Hastings, D. Rhodes, A.S. Fellerman, D. McKendrick, C. Dixon, New approaches for sludge management in the nuclear industry, Powder Technol. 174 (1–2) (2007) 18–24.
[9] A.P.G. Lockwood, J.R.L. Rumney, M.G. Barnes, J.M. Dodds, J. Peakall, T.N. Hunter, Approximation of hindered zonal settling rates for flocculated inorganic/organic composite suspensions in inertial flow conditions, J. Water Proc. Eng. 51 (2023) 103459.
[10] A.P.G. Lockwood, J. Peakall, N.J. Warren, G. Randall, M. Barnes, D. Harbottle, T. N. Hunter, Structure and sedimentation characterisation of sheared Mg(OH)2 suspensions flocculated with anionic polymers, Chem. Eng. Sci. 231 (2021) 116274.
[11] M. Johnson, J. Peakall, M. Fairweather, S. Biggs, D. Harbottle, T.N. Hunter, Characterization of multiple hindered settling regimes in aggregated mineral suspensions, Ind. Eng. Chem. Res. 55 (37) (2016) 9983–9993.
[12] P. Faia, R. Silva, M.G. Rasteiro, F. Garcia, Electrical tomography: a review of configurations, and application to fibre flow suspensions characterisation, Appl. Sci. 10 (7) (2020) 2355.
[13] R. Silva, P.M. Faia, F.A.P. Garcia, M.G. Rasteiro, Characterization of solid–liquid settling suspensions using Electrical Impedance Tomography: a comparison between numerical, experimental and visual information, Chem. Eng. Res. Des. 111 (2016) 223–242.
[14] C. Hu, L. Yu, D. Wang, H. He, Y. Li, Gas–liquid two-phase flow measurement by using electrical tomography sensors and Venturi, Flow Meas. Instrum. 102 (2025) 102763.
[15] J. Bux, J. Peakall, H.P. Rice, M.S. Manga, S. Biggs, T.N. Hunter, Measurement and density normalisation of acoustic attenuation and backscattering constants of arbitrary suspensions within the Rayleigh scattering regime, Appl. Acoust. 146 (2019) 9–22.
[16] A. Tonge, S. Usher, J. Peakall, S.O.l. Freear, D. Cowell, G. Franks, K. Mohanarangam, V. Ravisankar, M. Barnes, T.N. Hunter, Use of in situ acoustic backscatter systems to characterize spent nuclear fuel and its separation in a thickener, in: WM2019 Conference Proceedings. Waste Management Symposium 2019, WM Symposia, Phoenix, Arizona, 2019.
[17] H.P. Rice, M. Fairweather, J. Peakall, T.N. Hunter, B. Mahmoud, S.R. Biggs, Particle concentration measurement and flow regime identification in multiphase pipe flow using a generalised dual-frequency inversion method, Procedia Eng. 102 (2015) 986–995.
[18] A. Dash, W. Hogendoorn, C. Poelma, Ultrasonic particle volume fraction profiling: an evaluation of empirical approaches, Exp. Fluid 62 (4) (2021) 85.
[19] M. Guerrero, V. Di Federico, Suspended sediment assessment by combining sound attenuation and backscatter measurements – analytical method and experimental validation, Adv. Water Resour. 113 (2018) 167–179.
[20] F. Pedocchi, R. Mosquera, Acoustic backscatter and attenuation of a flocculated cohesive sediment suspension, Cont. Shelf Res. 240 (2022) 104719.
[21] P.D. Thorne, I.D. Lichtman, D. Hurther, Acoustic scattering characteristics and inversions for suspended concentration and particle size above mixed sand and mud beds, Cont. Shelf Res. 214 (2021) 104320.
[22] K.F.E. Betteridge, P.D. Thorne, R.D. Cooke, Calibrating multi-frequency acoustic backscatter systems for studying near-bed suspended sediment transport processes, Cont. Shelf Res. 28 (2) (2008) 227–235.
[23] P.D. Thorne, D.M. Hanes, A review of acoustic measurement of small-scale sediment processes, Cont. Shelf Res. 22 (2002) 603–632.
[24] R.J. Urick, The absorption of sound in suspensions of irregular particles, J. Acoust. Soc. Am. 20 (3) (1948) 283–289.
[25] L. Pang, X. Kong, H. Dong, Z. Zhang, L. Fang, Assessing particle size distribution in suspensions through a multi-frequency ultrasonic backscatter approach, Flow Meas. Instrum. 101 (2025) 102755.
[26] S.L. Brunton, B.R. Noack, P. Koumoutsakos, Machine learning for fluid mechanics, Annu. Rev. Fluid Mech. 52 (1) (2020) 477–508.
[27] I. Goodfellow, Y. Bengio, A. Courville, Deep Learning, MIT press, 2016.
[28] A. Krizhevsky, I. Sutskever, G.E. Hinton, Imagenet classification with deep convolutional neural networks, Adv. Neural Inf. Process. Syst. 25 (2012) 1097–1105.
[29] R. Yamashita, M. Nishio, R.K.G. Do, K. Togashi, Convolutional neural networks: an overview and application in radiology, Insights Imaging 9 (4) (2018) 611–629.
[30] A.L. Bowler, S. Bakalis, N.J. Watson, Monitoring mixing processes using ultrasonic sensors and machine learning, Sensors 20 (7) (2020) 1813.
[31] J.E. Escrig, A. Simeone, E. Woolley, S. Rangappa, A. Rady, N.J. Watson, Ultrasonic measurements and machine learning for monitoring the removal of surface fouling during clean-in-place processes, Food Bioprod. Process. 123 (2020) 1–13.
[32] A.L. Bowler, M.P. Pound, N.J. Watson, A review of ultrasonic sensing and machine learning methods to monitor industrial processes, Ultrasonics 124 (2022) 106776.
[33] A. Dwinovantyo, S. Solikin, H.M. Manik, T. Prartono, Susilohadi, Prediction and classification of suspended sediment and zooplankton signals from acoustic Doppler current profiler backscatter data using artificial neural networks, IOP Conf. Ser. Earth Environ. Sci. 944 (1) (2021) 012014.
[34] A.L. Gower, R.M. Gower, J. Deakin, W.J. Parnell, I.D. Abrahams, Characterising particulate random media from near-surface backscattering: a machine learning approach to predict particle size and concentration, EPL 122 (2018) 54001.
[35] A.S. Tonge, J. Peakall, D.M.J. Cowell, S. Freear, M. Barnes, T.N. Hunter, Experimental validation of acoustic inversions for high concentration profiling of spherical particles, using broadband technology in the Rayleigh regime, Appl. Acoust. 180 (2021) 108100.
[36] T.N. Hunter, J. Peakall, D. Egarr, D.M.J. Cowell, S. Freear, A.S. Tonge, L. Horton, H.P. Rice, I. Smith, K. Malone, D. Burt, M. Barnes, G. Randall, S. Biggs, M. Fairweather, Concentration profiling of a horizontal sedimentation tank utilising a bespoke acoustic backscatter array and CFD simulations, Chem. Eng. Sci. 218 (2020) 115560.
[37] H.P. Rice, M. Fairweather, T.N. Hunter, B. Mahmoud, S. Biggs, J. Peakall, Measuring particle concentration in multiphase pipe flow using acoustic backscatter: generalization of the dual-frequency inversion method, J. Acoust. Soc. Am. 136 (1) (2014) 156–169.
[38] Y. Wang, W. Li, T. He, C. Han, Z. Zhu, Z. Lin, The effect of solid particle size and concentrations on internal flow and external characteristics of the dense fine particles solid–liquid two-phase centrifugal pump under low flow condition, AIP Adv. 11 (8) (2021) 085309.
[39] E.M. Lakhdissi, I. Soleimani, C. Guy, J. Chaouki, Simultaneous effect of particle size and solid concentration on the hydrodynamics of slurry bubble column reactors, AIChE J. 66 (2) (2020) e16813.
[40] P. Puhan, A.K. Mukherjee, A. Atta, Insights into the influence of particle density and column inclination in polydisperse liquid–solid fluidized beds, Powder Technol. 425 (2023) 118540.
[41] A. Downing, P.D. Thorne, C.E. Vincent, Backscattering from a suspension in the near field of a piston transducer, J. Acoust. Soc. Am. 97 (3) (1995) 1614–1620.
[42] M.A. Ainslie, J.G. McColm, A simplified formula for viscous and chemical absorption in sea water, J. Acoust. Soc. Am. 103 (3) (1998) 1671–1672.
[43] A.P.G. Lockwood, G. Wadsley, N.J. Warren, J. Peakall, G.B. Webber, E.J. Wanless, D. Rhodes, M. Barnes, D. Harbottle, T.N. Hunter, Amphiphilic block copolymers as dual flocculation-flotation agents for rapid solid–liquid separation of radioactive wastes, Separ. Purif. Technol. 323 (2023) 124387.
[44] S.T. Hussain, T.N. Hunter, J. Peakall, M. Barnes, Utilisation of underwater acoustic backscatter systems to characterise nuclear waste suspensions remotely, Proc. Meet. Acoust. 40 (2020) 070005.
[45] S.T. Hussain, J. Peakall, M. Barnes, T. Hunter, Simultaneous velocity and concentration profiling of nuclear waste suspensions in pipe-flow, using ultrasonic Doppler and backscatter analysis, Proc. Meet. Acoust. 45 (2021) 070002.
[46] S.R. Dubey, S.K. Singh, B.B. Chaudhuri, Activation functions in deep learning: a comprehensive survey and benchmark, Neurocomputing 503 (2022) 92–108.
[47] C.E. Nwankpa, Advances in optimisation algorithms and techniques for deep learning, advances in science, Technol. Eng. Sys. J. 5 (5) (2020) 563–577.
[48] L.N. Smith, Cyclical learning rates for training neural networks, in: IEEE Winter Conference on Applications of Computer Vision (WACV), 2017, https://doi.org/10.1109/WACV.2017.58.
[49] G. Montavon, G.B. Orr, K.-R. Muller, Neural Networks: Tricks of the Trade, Springer Nature, Berlin, Heidelberg, 2012.
[50] L. Alzubaidi, J. Zhang, A.J. Humaidi, A. Al-Dujaili, Y. Duan, O. Al-Shamma, J. Santamaria, M.A. Fadhel, M. Al-Amidie, L. Farhan, Review of deep learning: concepts, CNN architectures, challenges, applications, future directions, J. Big Data 8 (1) (2021) 53.
[51] A.S. Tonge, J. Peakall, A.P.G. Lockwood, M. Barnes, T.N. Hunter, Characterizing flocculated mineral sediments with acoustic backscatter, using solid and hybrid scattering models, Ind. Eng. Chem. Res. 62 (42) (2023) 17328–17342.